PAPER

Check for updates

Formation of U(VI) peroxide nanoclusters from cascade reactions with a persulfate radical initiator

Vidumini S. Samarasiri,[a] Harindu Rajapaksha, [ID][a] Sarah McGee,[a] Sara E. Mason [ID][b] and Tori Z. Forbes [ID] *[a]

Radiolysis of water in high radiation fields generates a variety of reactive oxygen species that influence the chemical behavior and complexation of hexavalent uranium. This study investigates the behavior of interaction of a uranyl cation (UO_2^{2+}(VI)) with a series of free radicals that are formed *in situ via* activation of the free radical initiator persulfate ($S_2O_8^{2-}$), which releases both $SO_4^{•-}$ and $^{•}OH$ species in the solution. Electron Paramagnetic Resonance (EPR) and Raman spectroscopy were used to evaluate the presence of the hydroperoxyl radical ($HO_2^{•}$) and superoxide radicals ($O_2^{•-}$) that are formed within the solution through radical cascade reactions. In addition, a uranyl peroxide cluster solid (**NaU₂₄**) was crystallized and characterized using single crystal X-ray diffraction (SCXRD), vibrational spectroscopy, and EPR spectroscopy. The presence of the hydroperoxyl radical ($HO_2^{•}$) and superoxide radicals ($O_2^{•-}$) was also observed in the solid-state compound, but spectroscopic evidence suggests that it was associated with the Na^+ network and not the cluster itself. Density functional theory (DFT) calculations were also utilized to further confirm the radical species produced and determine the potential stabilization of radicals detected within the cluster and lattice.

Introduction

When aqueous solutions are subjected to ionizing radiation, a diverse array of free radicals are formed in the solvent that can react with actinide elements present in nuclear materials and influence their chemical behavior.[1] As a nuclear material emits ionizing radiation, nearby water molecules can undergo excitation or ionization reactions, resulting in reactive species such as $e_{aq}^{•-}$, $^{•}OH$, $H^{•}$, and $HO_2^{•}$ radicals.[2] Additional reactions with other water molecules, free radicals, or dissolved oxygen can result in the formation of reactive oxygen species (ROS), such as peroxide (O_2^{2-}), the hydroperoxyl anion (OOH^-), hydrogen peroxide (H_2O_2), and the superoxide anion radical ($O_2^{•-}$).[1] These species can influence the redox behavior of actinides, such as uranium, thereby influencing the corrosion of fuel pellets,[3] hampering radiochemical separations,[4–7] and creating soluble actinide phases that will influence environmental fate and transport.[8–10]

In addition to changes in the oxidation state, free radicals formed during water radiolysis may complex with the actinide cation, changing the chemical speciation and overall behavior of the system. For example, McNamara *et al.* reported that the

[a]Department of Chemistry, University of Iowa, Iowa City, 52242, UK.
E-mail: tori-forbes@uiowa.edu
[b]Center for Functional Nanomaterials, Brookhaven National Laboratory, Upton, NY 11973, USA

uranyl peroxide phase, studtite, $(((UO_2)O_2(H_2O)_2) \cdot 2H_2O)$ was formed on the surface of spent nuclear fuel due to alpha radiolysis of water.[11,12] Sattonnay *et al.* also discovered that metastudtite, $((UO_2)O_2(H_2O)_2)$, formed on the surface of UO_2 after irradiation with alpha particles, which again takes place through the *in situ* production of H_2O_2 through radiolysis of water.[13] More recent studies by Kravchuk *et al.* and Scherrer *et al.* indicated that the $O_2^{•-}$ radical can be stabilized within U(VI) triperoxide coordination complexes and Lottes *et al.* suggested that $^{•}OH$ radicals are incorporated into U(VI) peroxide clusters formed through hydrothermal methods.[14–16]

The major challenge with understanding radicals and reactive species produced during irradiation studies is the complex mixture of radiolysis products that are formed during exposure to α or γ radiation; thus, we have previously utilized chemical radical initiators to initially simplify the system. Kravchuk *et al.* and Scherrer *et al.* created peroxyl radicals *in situ* through the autoxidation of benzaldehyde in benzyl alcohol to understand the behavior of superoxide in these systems.[17,18] This previous work demonstrated the direct coordination of the superoxide radical to the U(VI) cation, suggested increased stability of the radical in solution, and indicated that the superoxide anion engaged in additional cascade reactions with other substrates (*e.g.* CO_2 from direct air carbon capture and the formation of PO_4^{3-} from an aminophosphonate ligand).[14,19] This work demonstrated that fundamental knowledge regarding interactions between actinide metal cations

and radiolysis products can be gained from using chemical radical initiators.

In this study, we set out to expand our understanding of U(VI) interactions with ROS species by turning our attention to the ˙OH radical through the use of persulphate ($S_2O_8^{2-}$) as the chemical initiator. Persulphate is widely utilized in advanced oxidation processes due to its ability to form sulphate radicals ($SO_4^{•-}$)[20,21] through activation by heat, UV light, transition metals, and microwave irradiation.[21–24] Upon activation under neutral and basic conditions, persulphate triggers a secondary reaction, leading to the formation of ˙OH radicals in solution.[20,25,26] For the current work, the behavior of U(VI) in the presence of activated persulfate was explored using Raman spectroscopy and electron paramagnetic resonance (EPR) spectroscopy. Through these experiments, we successfully isolated a solid-state material (**NaU$_{24}$**), which was further characterized using single-crystal X-ray diffraction, Raman spectroscopy, and EPR spectroscopy. Additionally, density functional theory (DFT) calculations were conducted to confirm the intermediate complexes and free radical species formed throughout the radical cascade.

Experimental methods

Solution conditions for the persulfate reaction with U(VI)

The persulfate activation was initiated by adding 2.5 ml of 0.5 M sodium persulphate (Alfa Aesar, 99%) and 2.5 ml of a 0.3 M sodium fumarate (Alfa Aesar, 99%) buffer to a 20 ml scintillation vial and heating to 70 °C for one hour. At this point, 0.2 ml of 0.02 M uranyl nitrate hexahydrate (Bio-Analytical Industries Inc., 99%) dissolved in water was added to the activated solution and the pH of the reaction mixture was measured at 7.5. *CAUTION: This synthesis contains radioactive ^{238}U; therefore the experiments were performed by trained personnel in a licensed research facility with special precautions taken during handling, monitoring, and safe disposal of radioactive materials.* The scintillation vial was then capped and allowed to age over a course of three weeks in the dark. Light yellow blocky crystals appeared in the bottom of the vial within 3 weeks and reached the maximum production of the solid occurring within 4 weeks.

Single-crystal X-ray diffraction

Structural characterization of the resulting solid material (**NaU$_{24}$**) was performed using single-crystal X-ray diffraction. A subsample of the product was placed on a glass slide, isolated from the mother liquor, and coated with NVH immersion oil. High-quality single crystals were isolated and mounted on a Bruker Quest single-crystal X-ray diffractometer equipped with Mo Kα radiation (λ = 0.7107 Å), CMOS detector, and a low temperature cryostat (Oxford Cryosystems, Cryostream 800) set at 100 K. All diffraction data were collected, integrated, and corrected (*i.e.* Lorentz, polarization, absorption and background effects) using the Bruker APEX4 software.[27] Structure determination was performed using direct methods and least

squares refinement of the partial structure was conducted using APEX4 software.[27] U atoms were located during the initial structure determination and the O and Na atoms were observed in the residual electron density map following refinement of the partial structure. The O atoms associated with the U$_{24}$ cluster were well resolved and could be refined anisotropically in all cases. Na 1, 2, and 3 were also refined in discrete positions, but Na 4, 5, and 6 were more disordered and the atoms were prolate when refined anisotropically. Disorder for Na5 could be modeled using a split site with a partial occupancy of 0.125. Final modeling of the partial occupancy for the Na sites was also compared to the charge balancing requirement of the overall compound formula. Oxygen atoms associated with water and hydrogen peroxide in the interstitial lattice region were well resolved but could not be refined anisotropically. Two positions (O20 and O24) were disordered and modeled as split sites with partial occupancy. Hydrogen atoms were not included in the structural model due to difficulties in locating the positions in the residual electron density map. The Crystallographic Information File for **NaU$_{24}$** can be found in the Cambridge Structural Database by requesting number 2433767.

Raman spectroscopy

Raman spectra were collected for relevant solutions including the initial reagents and the mother liquor over a 3-week crystallization period. Aliquots of the solution were placed into glass vials and the solution phase Raman spectra were collected using an SnRI High Resolution Sierra 2.0 Raman spectrometer equipped with 785 nm laser energy and a 2048 pixel TE cooled CCD detector that measured data from 200 to 2000 cm^{-1}. Data were collected in multi-acquisition mode by averaging three spectra with an acquisition time of 5 seconds and the maximum power of the excitation laser at 15 mW. Solid-state Raman spectroscopy was also performed on single crystals isolated during structural characterization of the product. These crystals were transferred to a glass slide and placed under a ReniShaw inVia Raman microscope. Both the unwashed and hexane washed crystalline products were analyzed by Raman spectroscopy. Samples were imaged under a confocal microscope at 50× magnification and then the data were collected using a 785 nm excitation source operating at its highest power at 15 mW. The 1200 mm grating results in a resolution of 2 cm^{-1} over a scan range of 200–2000 cm^{-1}. Data were acquired in multi-acquisition mode where the spectra were automatically reiterated three times. Both solid-state and solution spectra were background-subtracted and fitted using the peak analysis protocol in OriginPro 9.60 (OriginLab, Northampton, MA) 64-bit software. Lorentzian or PseudoVoigt functions were employed in fitting peaks and the fitting parameters converged to χ^2 values of less than 10^{-6}.[28]

Infrared spectroscopy

IR spectra of the solid-state materials formed during the reaction were collected with a Bruker VERTEX 70v FTIR spectrometer equipped with a platinum ATR microscope objective.

The spectra were collected in the region of 500–4000 cm^{-1} region and the IR bands were fitted with Lorentzian and Gaussian functions with χ^2 converged to values of less than 10^{-6} using OriginPro 2024 software.

Electron paramagnetic resonance spectroscopy

Both solid and solution samples were analyzed using electron paramagnetic resonance spectroscopy. Approximately 10 mg of the isolated crystals were placed into a 5 mm quartz EPR tube for analysis of the solid-state materials. For solution studies, the solid product was dissolved in 1 ml of water and 100 mM DMPO (5,5-dimethyl-1-pyrroline-*N*-oxide) was added as the spin trap. In both cases, room temperature EPR spectroscopic data were collected on a Bruker EMX spectrometer equipped with an HS EPR cavity. The magnetic field was centered at 3509 G with a microwave frequency of 9.854 GHz at 20.00 mW power. The sweep width was 80.00 G and the sweep time was 20.972 s with an 81.920 ms signal channel. The receiver gain was equal to 1.00 × 10^5 and the modulation frequency and amplitude were 100 kHz and 1.00 G, respectively. All spectra were collected in the additive mode using 50 scans. Observed signals were integrated using the Bruker WIN-EPR acquisition software (V. 4.33.12.50.1 2008) and data were plotted using OriginPro 2024 software.

DFT calculations

The Gaussian 16[29] software package was used to perform all geometry optimizations on molecular species. The B3LYP (Becke, 3-parameter, Lee–Yang–Parr)[30,31] hybrid function was used to model exchange correlation effects and van der Waals dispersion correction methods DFT-D3 with the Becke–Johnson damping term were also utilized.[32] A polarized triple zeta (def2-TZVP)[33] basis set was utilized to represent the O, H, and S atoms, while the SDD effective core potential and the corresponding valence basis sets were used to represent U atoms.[34,35] All structures were optimized with no symmetry constraints to a tight convergence criterion with a Root Mean Square (RMS) force criterion of 1 × 10^{-5} Hartrees per radian. Results of calculated vibrational frequencies from these geometric optimizations were monitored to ensure that structures were optimized to a true minimum with no imaginary frequencies. When calculating reaction energies, the Conductor-like Polarizable Continuum solvation Model (CPCM)[36,37] with water as the solvent was used during both geometry optimization and in final single point calculations.

Single point calculations with the Gaussian 16 optimized structure were performed to determine the theoretical g-value using ORCA 6.0.1.[38] B3LYP hybrid functionals were used in these calculations,[30,31] and relativistic effects were included by the Zeroth-Order Regular Relativistic Approximation (ZORA)[39,40] in combination with ZORA-recontracted[41] versions of the def2 basis sets.[42,43] The H, O, and S atoms were represented using the ZORA-def2-TZVP basis set while U atoms were represented using the SARC-ZORA-TZVP basis set together with SARC/J coulomb-fitting auxiliary basis sets.[41–43] Tight SCF convergence was used throughout the calculations

of all EPR parameters. Visualization of spin densities was conducted using the Chemcraft program.[44]

Results and discussion

Characterization of the initial reaction in solution

The addition of U(VI) to the activated persulfate solution initially resulted in the formation of a clear solution that then formed a crystalline product upon aging. Persulphate (S$_2$O$_8^{2-}$) was chosen as a chemical initiator because it readily forms sulfate radicals (SO$_4^{2\bullet-}$) with heat, UV light, transition metals, alkalis, ultrasound or microwaves[45] (rxn (1)) that react with water to create reactive oxygen species. Within aqueous solutions the sulfate radicals can further react with water to form sulphate anions and hydroxide radicals (rxn (2)). After thermal activation of the persulphate, the addition of uranyl nitrate changes the color of the resulting solution to light yellow, but overall, the mixture remains transparent. This solution is stable over the course of approximately three weeks, wherein a solid crystalline material begins to form on the bottom of the vial. The formation of crystalline materials continued for four weeks, where total yields of the solid product were 80–85% based on U.

$$S_2O_8^{2-} \rightarrow 2SO_4^{\bullet-} \tag{1}$$

$$SO_4^{\bullet-} + H_2O \rightarrow H^+ + SO_4^{2-} + {}^{\bullet}OH \tag{2}$$

To confirm the activation of the persulfate in solution, we first evaluated the reaction mixture over time using Raman spectrometry (Fig. 1a and Table S1). Raman spectra of the initial solution after heating contained five bands in the spectral region of interest (700–1200 cm^{-1}). The most intense feature at 1077 cm^{-1} was associated with the S–O stretching in S$_2$O$_8^{2-}$ whereas peaks at 835 and 801 cm^{-1} represent hydrolyzed products such as peroxomonosulfate (SO$_5^{2-}$), confirming the activation of the radical initiator.[46,47] Additional features at 904 and 981 cm^{-1} are associated with C–C stretching vibrations[48] of the fumarate molecule, but we also note that SO$_4^{2-}$ is also observed at approximately 980 cm^{-1} as well.[46] The band at 819 cm^{-1} corresponds to the ν_1 uranyl symmetric stretching of the UO$_2^{2+}$ cation that results from the addition of the uranyl nitrate to the solution. Normally an acidic solution that contains uranyl nitrate would have a band at 870 cm^{-1}, corresponding to the uranyl pentaaqua species; however, the ν_1 mode in the U(VI) persulfate solution is red shifted by 50 cm^{-1}.[49–51] As the solution pH for the activated persulphate is near neutral, uranyl hydrolysis can cause a red shift for the ν_1 uranyl stretching band.[52] Alternatively, the presence of the chelating fumarate molecule may also result in the observed changes in the spectral features.

Aging the U(VI)-bearing solution resulted in subtle changes in the Raman spectrum over time. After one week, the same features were observed within the spectral window of interest; however, there is a significant increase in the intensity and sharpness of the peak at 984 cm^{-1} and a red shift in the U(VI)
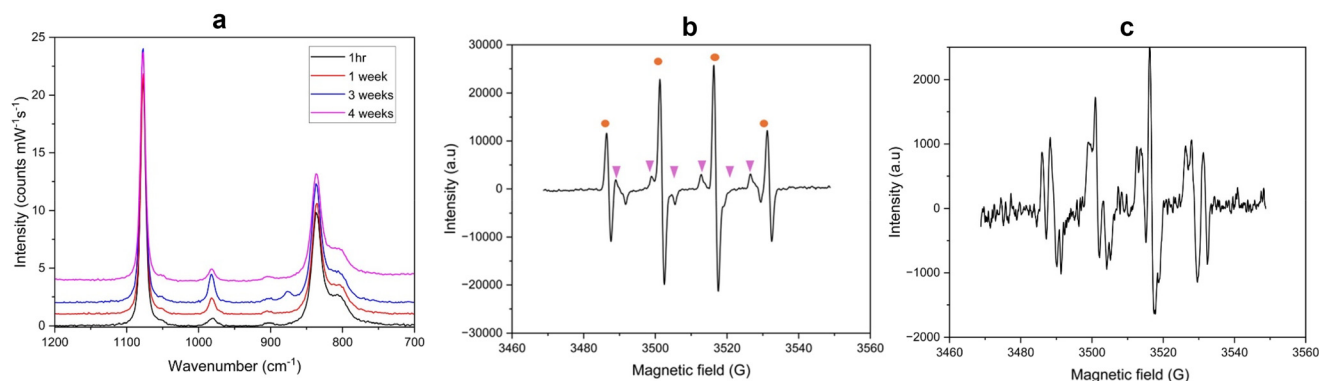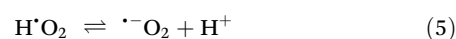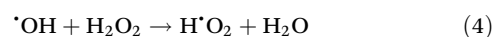
Fig. 1 (a) Raman spectra of the initial solution containing uranyl nitrate, sodium persulfate and sodium fumarate after aging for 1 h, 1 week, 3 weeks and 4 weeks. (b) EPR spectrum of the initial reactants with 100 mM DMPO added as a spin trap agent. The orange circles correspond to the presence of the $^\bullet$OH radical and pink triangles indicate the presence of sulphate radicals. (c) EPR spectrum of the reaction mixture when the solid product appears in the solution (after 4 weeks) indicates a mix of radical species that includes $^\bullet$OH and $O_2^{\bullet-}$ species.

ν_1 symmetry mode by 6 cm^{-1}. Changes in the band at 984 cm^{-1} are likely attributed to the gradual conversion of persulphate to sulphate over time, whereas the shift in the U(vi) mode corresponds to change in the coordination environment around the metal cation. After 3 weeks, we see the ingrowth of a peak at 877 cm^{-1} that we attribute to the formation of free H$_2$O$_2$ within the reaction medium. This spectral feature then disappears upon the formation of a solid yellow product at 4 weeks of aging the reaction solution. Given the appearance of a peak at 813 cm^{-1} in the U(vi) containing solution and evidence of peroxide formation, the solution Raman data suggest the formation of a U(vi) peroxide nanocluster in solution prior to crystallization.

The EPR spectra of the activated persulphate solution and 100 mM DMPO spin trap contain two splitting patterns that were deconvoluted to identify the free radicals present in the solution (Fig. 1b). We have identified DMPO-SO$_4$ adducts with a 1 : 1 : 1 : 1 splitting (A_N = 13.84 and A_H = 10.08, 1.48) and DMPO-OH adducts with a 1 : 2 : 2 : 1 splitting ($A_H = A_N$ = 14.89) as the two major contributors to the spectra. EPR spectral features for the initial solutions also matched those proposed by Yang *et al.* when the persulphate system was activated through interaction with vanadium complexes.[53] The hyperfine splitting constants also matched the values for the DMPO adducts reported by Buettner *et al.*, where for DMPO-OH, $A_H = A_N$ at 14.9 G, and for DMPO-SO$_4$ A_N = 13.82 and A_H = 10.1, 1.42.[54,55] These results indicated that the expected SO$_4^{\bullet-}$ and $^\bullet$OH radicals are generated during the persulphate activation in the system. After the formation of the solid product (4 weeks), the solution was again analyzed using EPR spectroscopy and the DMPO spin trap. The analysis revealed the presence of a mixture of SO$_4^{\bullet-}$, $^\bullet$OH, and O$_2^{\bullet-}$ radicals, (Fig. 1c) with the presence of O$_2^{\bullet-}$ confirmed by the hyperfine splitting constants (A_N = 14.39 G and A_H = 11.30 G).[54,56]

Our results support previous work indicating that a cascade reaction occurs in the presence of aqueous persulfate at neutral and alkaline pH when the reaction is activated by

heat,[21,57,58] but it is further modified by the presence of U(vi). EPR spectroscopy clearly demonstrates the formation of SO$_4^{\bullet-}$ and $^\bullet$OH radicals in the initial solution, which according to kinetic studies performed by Johnson *et al.* is the initial reaction and is the rate-determining step.[21] Previous work also indicated that other sulfur-based radicals (*e.g.* SO$_5^{\bullet-}$ and SO$_3^{-\bullet}$), may also be generated, but we found no evidence of their formation in our experiments.[59] After the initial reaction, SO$_4^{\bullet-}$ and $^\bullet$OH radicals generated *in situ* can either complex with the U(vi) cation or further react with water or other co-solutes in the solution. There are no obvious changes in the Raman spectra to suggest that there is a change in speciation for the U(vi) cation; however, there is significant overlap in the spectral features of the radical initiators and the U(vi) symmetric stretch that precludes us from confirming this fact. The Raman spectra exhibit an additional feature at 875 cm^{-1} after three weeks of aging that corresponds to free H$_2$O$_2$ in the system. Formation of peroxide can be rationalized by interactions between the $^\bullet$OH radicals formed through the initial persulfate decomposition (rxn (3)) or alternatively, the hydroxide radicals can also interact with the H$_2$O$_2$ produced within the system to form hydroperoxyl (HO$_2^\bullet$) radicals (rxn (4)). The hydroperoxyl radical can then undergo deprotonation to form the superoxide radical (O$_2^{\bullet-}$) (rxn (5)), demonstrating that a range of reactive oxygen species can be formed under these conditions.

$$2^\bullet OH \rightarrow H_2O_2 \tag{3}$$

$$^\bullet OH + H_2O_2 \rightarrow H^\bullet O_2 + H_2O \tag{4}$$

$$H^\bullet O_2 \rightleftharpoons {}^{\bullet-}O_2 + H^+ \tag{5}$$

This mechanistic reasoning indicates that O$_2$ gas is not necessary for the formation of peroxide; however, additional reactions performed under N$_2$ gas showed no evidence of significant H$_2$O$_2$ ingrowth in the Raman spectrum (Fig. S1 and S2). This result leads us to conclude that peroxide is generated

in situ when the sulfate radicals initiate the cascade reaction and the presence of O_2 gas is necessary for its formation. The importance of dissolved oxygen has been previously noted in irradiation studies by Jegou *et al.*, where aerated solutions substantially increase the presence of H_2O_2 in the system compared to those purged with argon gas because of interactions of the solvated electron with dissolved O_2 gas.[60] However, a solvated electron is not generated during the activation of the persulphate radical initiator, suggesting that a different mechanism must be in play for the current system.

Build-up of peroxide to levels that are observable by Raman spectroscopy occur weeks after initiation of the experiment and this spectral feature does not occur unless U(VI) is present in the system. This result suggests that peroxide formation occurs after the initial persulphate activation step and the presence of the actinide cation may also influence the radical initiator. Previous work on persulfate chemistry indicated that transition metals can also activate the molecule through a one-electron reduction step and we have previously noted the presence of trace metals in our U(VI) peroxide systems.[18,61] While we cannot entirely rule out trace metals in this system, the overall yield of the peroxide makes other mechanisms more likely. The formation of U(VI) peroxide has also previously been linked to photochemical reactions;[62–65] however, aging of the U(VI) persulfate solutions occurred in the dark, confirming that the formation of peroxide did not occur through a photochemical mechanism.[66] After four weeks, the peroxide signal disappeared from the Raman spectra, and this can be traced to the consumption of the U(VI) and the formation of a solid product.

Identification of the product

The solid crystalline product that formed from the persulfate radical initiator was initially characterized by single-crystal X-ray diffraction and structural determination of the solid indicated the presence of U(VI) peroxide clusters (Fig. 2a). Selected crystallographic information and bond distances are provided in SI Tables S2 and S3, respectively. The molecular clusters identified by structural characterization consisted of 24 U(VI) cations bound to two oxygen atoms to create the nearly linear dioxo uranyl cation (UO_2^{2+}) with axial U=O bond distances ranging from 1.787(10) Å to 1.819(11) Å. Each uranyl cation is further bound to two $\mu_2\text{-}O_2^{2-}$ and two OH^- ligands within the equatorial plane to create an overall hexagonal bipyramidal coordination about the U(VI) cation. Average equatorial U–O bond distances range between 2.334(8) and 2.457(10) Å and peroxide anions contain O–O bond lengths of 1.473(10) and 1.479(11) Å, which are comparable to the ~1.5 Å bond distance that is commonly observed in solid state peroxides.[67,68] The uranyl complexes link together into tetrameric and hexameric rings and create the larger molecular cluster with a sodalite topology and overall formula of $[(UO_2)_{24}(OH)_{24}(O_2)_{24}]^{24-}$ (U_{24}).

The U_{24} species was one of the first characterized uranyl peroxide molecular clusters and has since been identified as one of the most common species to exist in solution. Discovered by the Burns group in 2005, the cluster was synthesized by combining uranyl nitrate with 30% H_2O_2 in LiOH.[68] These clusters have since been observed as a primary product in the self-assembly of monomeric species and as the breakdown product of other uranyl peroxide clusters (*i.e.* U_{28} and U_{60}).[69,70] The Li-U_{24} complexes have also been studied using a range of chemical techniques that demonstrate the stability of uranyl peroxide clusters in aqueous solutions and the importance of the Li^+ counter cations trapped within the cage structure.[71,72] Cation exchange of the Li-U_{24} species can occur through the addition of saturated sodium acetate. Overall yields of the Na^+ bearing U_{24} material using the cation exchange method were reported to be approximately 30% and it crystallizes in a monoclinic, $C2/m$ space group with $a =$
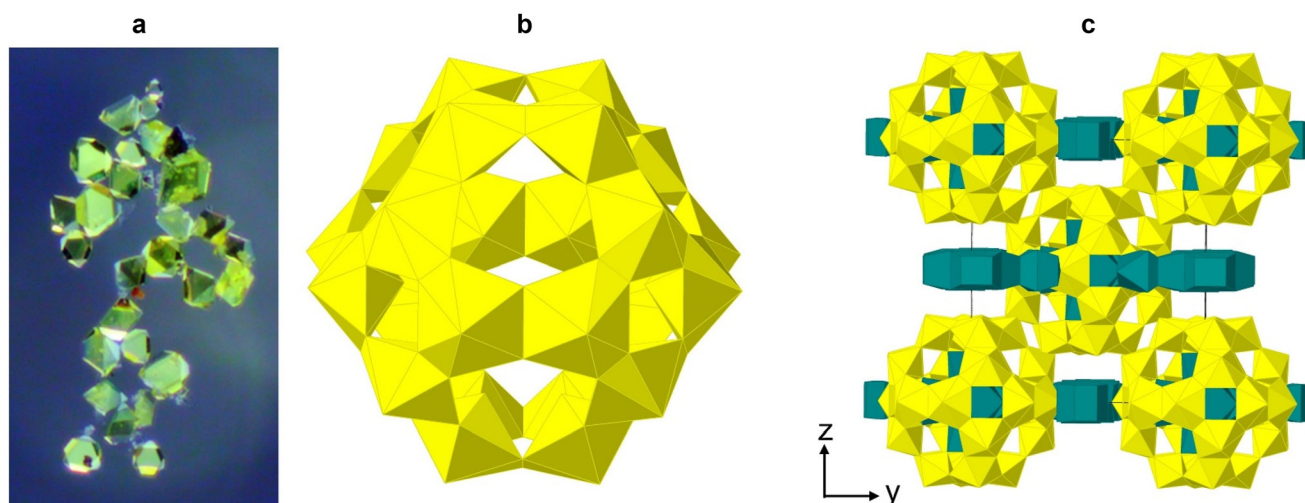

Fig. 2 (a) **NaU₂₄** crystals are formed after aging the U(VI) containing activated persulfate solution for four weeks. (b) The NaU₂₄ solid contains $[(UO_2)_{24}(OH)_{24}(O_2)_{24}]^{24-}$ molecular clusters in the crystalline lattice. U(VI) positions are represented as yellow polyhedra to build the overall U_{24} cluster. (c) The U_{24} molecular clusters are ordered within the crystalline lattice and are charge balanced by networks of Na^+ cations (teal polyhedra). Only the ordered Na^+ networks are shown as additional disordered Na^+ cations and water molecules have been removed for clarity.

26.184(2) Å, b = 26.175(2) Å, c = 18.415(2) Å, and β = 132.259°. Structural characterization of this compound indicated that the formula was $Li_2Na_{16}[Na_6(H_2O)_8][(UO_2)_{24}(OH)_{24}(O_2)_{24}]\cdot72H_2O$.[73,74] Zanonato *et al.* also reported a Na-U$_{24}$ species during the exploration of F$^-$ doping of the uranyl peroxide clusters that crystallizes in the tetragonal $I4/m$ space group with a = 19.3480(8) Å and c = 25.551(4) Å.[75]

The compound formed in this current study crystallizes with different unit cell parameters than the previously reported structures (tetragonal $I4/m$, a = 19.7190(5) Å and c = 22.1550(9) Å) and this change is caused by differences in the Na$^+$ network (Fig. 2c). A $Na_6(H_2O)_8$ core (Na(1) and Na(2)) occurs within the center of the U$_{24}$ cluster and is identical to the previous Na-bearing U$_{24}$ solids (Fig. 3a). However, the arrangement of the alkali cations on the exterior of the cluster differs between the previous solid and the one characterized herein (Fig. 3b). In the Na-U$_{24}$ clusters reported by Nyman,[73,74] the Na$^+$ cations are linked through bridging H$_2$O molecules and a central Li$^+$ tetrahedron to form a linear pentameric chain within the interstitial regions. Three crystallographically unique Na$^+$ cations are observed on the exterior of the cluster reported by Zanonato *et al.* but the crystallographic information file is unavailable for further analysis of the structural differences in the sodium network.[75] In the current Na-U$_{24}$ cluster, only Na$^+$ is

observed on the exterior of the clusters and forms an octameric unit through both bridging H$_2$O and peroxide units (O–O distance 1.57(7) Å) that are captured by the Na$^+$ cation. This is similar to the presence of H_2O_2/HO_2 in the potassium network that surrounds the U(VI) peroxosuperoxo complex (KUPS) previously reported by Kravchuk *et al.*, which was synthesized through the use of benzaldehyde as the radical initiator.[14] Based on the structural characterization of the material, we determined that the overall formula of the compound is $Na_{10}(Na_6(H_2O)_8Na_8(H_2O)_{22}(H_2O_2)_4)$ $[(UO_2)_{24}(OH)_{24}(O_2)_{24}]\cdot22H_2O$.

To further explore the composition of the solid-state material, a Raman spectrum was collected from **NaU$_{24}$** single crystals that were formed from the activated persulfate solution. The spectrum featured four prominent peaks, where the band at 798 cm^{-1} was assigned to the ν_1 uranyl symmetric stretching of UO_2^{2+} and the two broad bands at 816 and 845 cm^{-1} correspond to ν_2 and ν_1 stretching of O_2^{2-} bound to U (Fig. 4a). These features agree well with the previously reported Raman-active bands for U$_{24}$ that have been previously reported by Burns *et al.*[76] A shoulder at 856 cm^{-1} confirms the presence of H$_2$O$_2$ within the solid-state material. Bands for pure Na$_2$O$_2$ are observed at 736 cm^{-1}, so the peak at 857 cm^{-1} likely corresponds to a O–O stretch associated with a hydrated
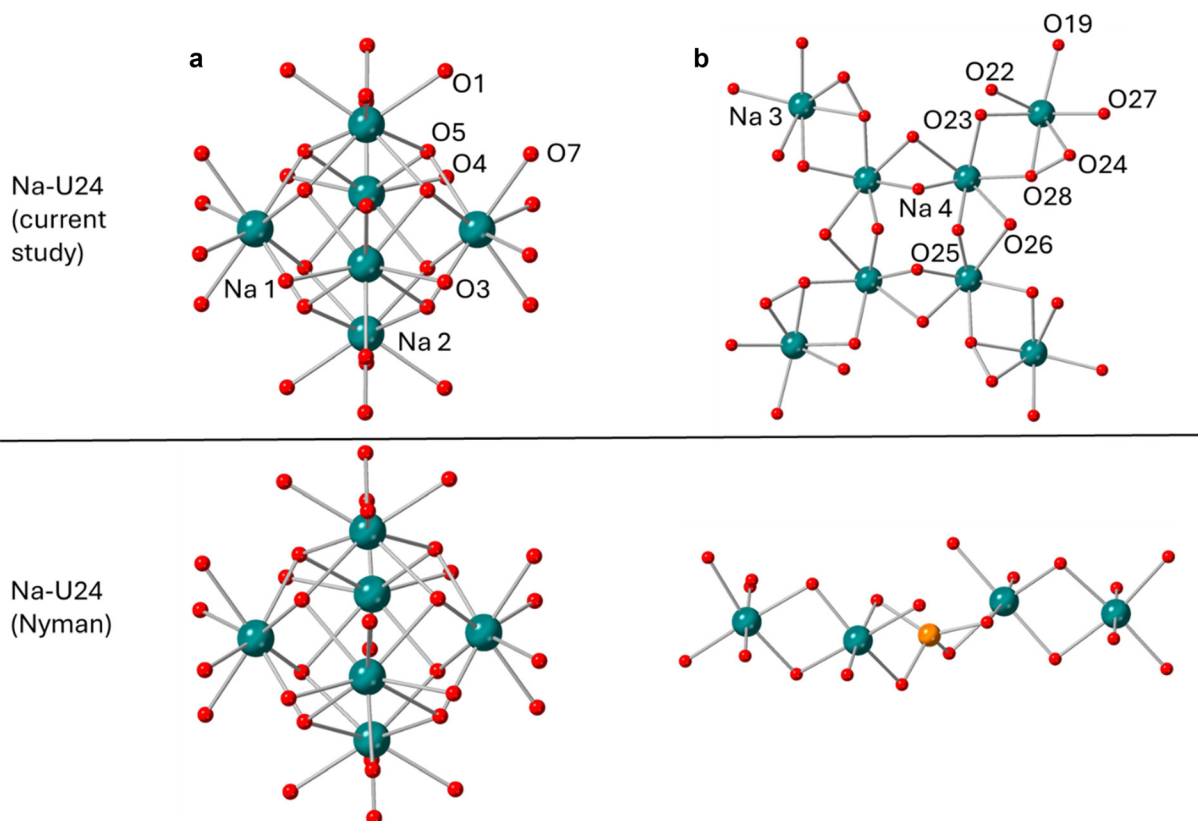

Fig. 3 (a) Arrangement of the $Na_6(H_2O)_8$ core in the NaU$_{24}$ compound isolated from the activated persulfate mixture (top) is identical to the core observed in the previous work by Nyman[73,74] (bottom). (b) The cation network in the **NaU$_{24}$** compound isolated herein contains a Na$^+$ octamer that also contains H$_2$O$_2$ molecules (top). The previous work by Nyman[73,74] includes chain structures of both Na and Li cations (bottom). Na atoms, O atoms and Li atoms are given in teal, red and orange, respectively.
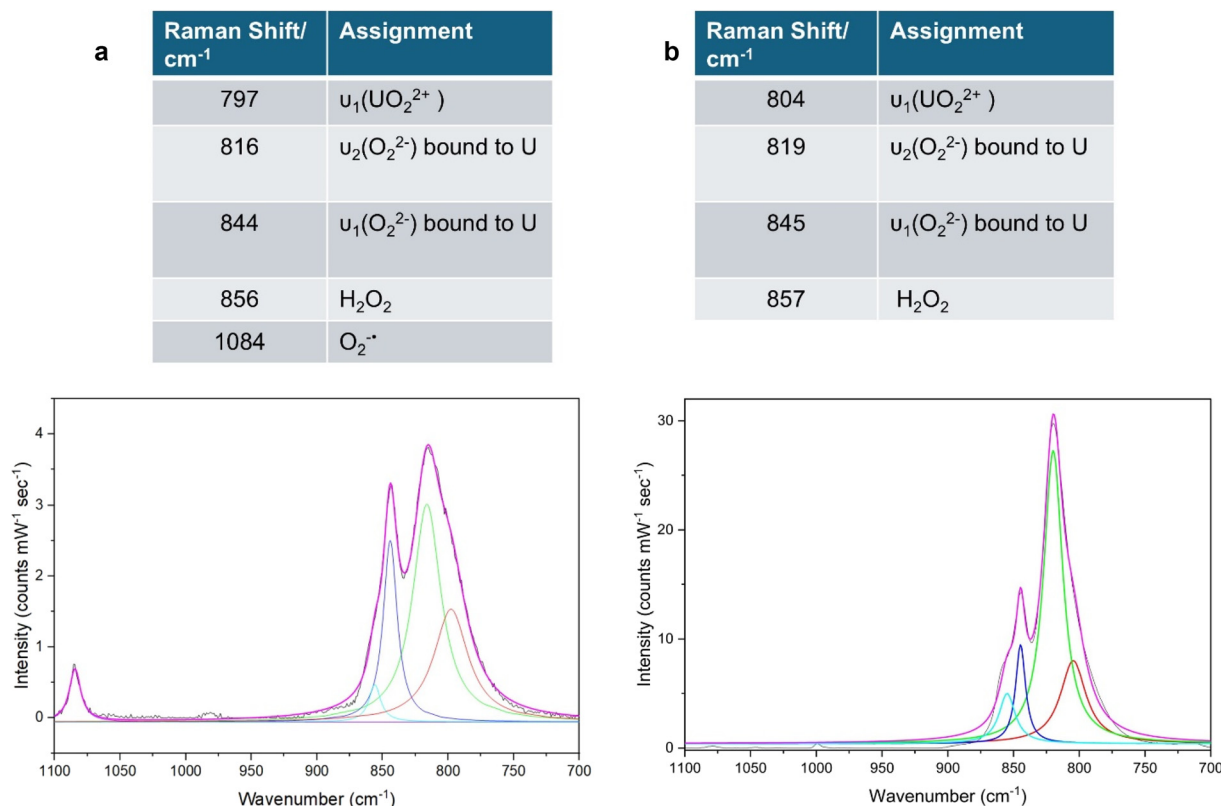
a

Raman Shift/ cm^{-1}	Assignment
797	$\nu_1(UO_2^{2+})$
816	$\nu_2(O_2^{2-})$ bound to U
844	$\nu_1(O_2^{2-})$ bound to U
856	H_2O_2
1084	$O_2^{\bullet-}$

b

Raman Shift/ cm^{-1}	Assignment
804	$\nu_1(UO_2^{2+})$
819	$\nu_2(O_2^{2-})$ bound to U
845	$\nu_1(O_2^{2-})$ bound to U
857	H_2O_2

Fig. 4 (a) Raman spectra of the solid NaU$_{24}$ cluster as synthesized and (b) after being washed with hexane show a decrease in the band at 1084 cm^{-1} and a relative increase in the band at 857 and 819 cm^{-1}.

peroxide form.[77] The band at 1084 cm^{-1} could be attributed to residual solvent or $O_2^{\bullet-}$/ HO$_2^{\bullet}$ as the literature suggests the Raman peak for free superoxide to be near 1090 cm^{-1} in alkali halide lattices.[78,79] In addition, Stoin *et al.* reported the *in situ* generation of NaO$_2$ in concentrated NaOH leads to a band in the Raman spectra at 1082 cm^{-1}.[80] However, Na$_2$CO$_3$ also contains a major feature at 1080 cm^{-1}[80] and uranyl peroxides are known to engage in direct air carbon capture.[14,19] Once the solid crystals were washed with hexane, the peak at 1084 cm^{-1} disappeared and the intensity of the peaks at 857 and 819 cm^{-1} increased compared to the uranyl symmetric stretching band (Fig. 4b). This suggests that during the washing step, the solvent is removed or $O_2^{\bullet-}$ radical may have reacted with the solvent and formed the HO$_2^-$ molecule.

Solid-state IR spectra of the unwashed samples also contain evidence of the hydroperoxyl radical (Fig. S3–S8). More specifically, features at 3453, 1394, and 1145 cm^{-1} agree well with previous literature results for HO$_2^{\bullet}$.[81] In addition, there is evidence of H$_2$O$_2$ in the lattice with features at 3220, 2852, 1415, 1377, and 892 cm^{-1}.[82] In addition, the uranyl antisymmetric stretch can be identified at 915 cm^{-1} and ligated peroxide stretching features at 861 and 852 cm^{-1}, which is comparable to previously reported values for U(VI) peroxide clusters.[83] Thus, the IR spectrum provides additional evidence that the **NaU$_{24}$** compound contains the hydroperoxyl radical and H$_2$O$_2$ in the solid-state lattice.

To further confirm the presence of HO$_2^{\bullet}$ in the solid-state phase, EPR spectra were also collected on the solid-state material (Fig. 5a). A single, weak isotropic signature can sometimes be observed for **NaU$_{24}$** at $g = 2.019$ but it is not consistently reproducible. The g value for solid state KO$_2$ is found at $g = 2.04$ but the g tensor varies from 2.015–2.106 depending on the coordination environment.[84] In addition, the g_{iso} value for the HO$_2^{\bullet}$ radical has previously been reported at 2.016, which is in agreement with what is observed in the **NaU$_{24}$** solid.[85] The EPR signature is different from what is observed for the U(VI) triperoxide species ($g_\perp = 2.017$ and $g_\parallel = 2.05$) and for the extended U(VI) peroxide, studtite [UO$_2$(O$_2$)(H$_2$O)$_2$]·2H$_2$O ($g_\perp = 2.014$ and $g_\parallel = 2.039$) as both typically contain an axial signature when the free radical is complexed to the metal cation.[14,15,18] We have noted in previous work that the $g_\parallel$ is sometimes so weak that it cannot be readily observed from the background,[18] but the features in this previous U(VI) superoxide study are broader than what is observed within the solid state **NaU$_{24}$**. Lottes *et al.* have previously reported the presence of a radical in the U$_{60}$Ox$_{30}$ cluster with an isotropic $g = 2.016$, which they suggested was linked to an $^{\bullet}$OH located within the U(VI) cluster itself.[16] Overall, the solid-state EPR spectra confirms the presence of an oxygen free radical (most similar to HO$_2^{\bullet}$) but does not definitely locate it specifically within the U$_{24}$ cluster or the charge balancing Na$^+$ network.

To further explore the behavior of the free radical within the **NaU$_{24}$** solid, the crystals were dissolved in water for
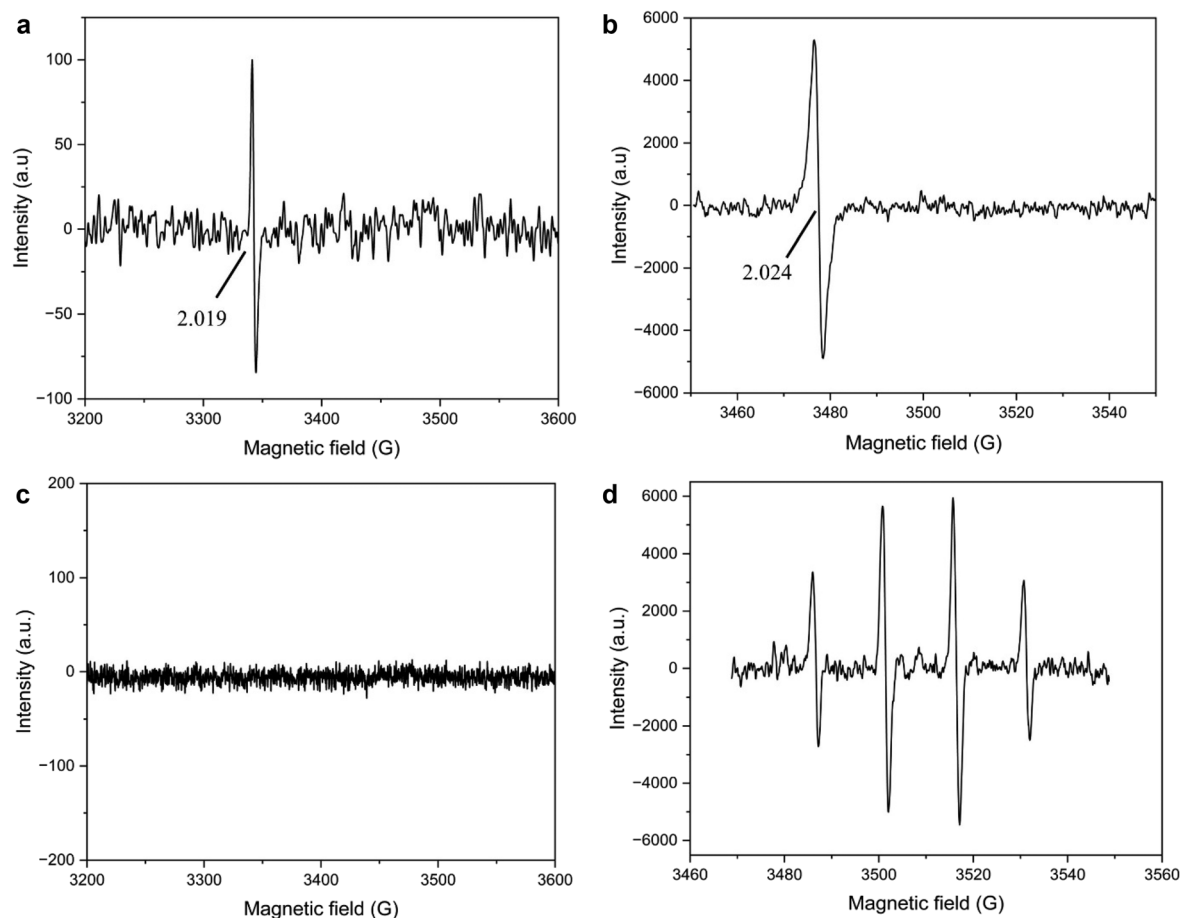
Fig. 5 EPR spectra are reported for (a) solid **NaU$_{24}$**, (b) **NaU$_{24}$** dissolved in water, (c) **NaU$_{24}$** dissolved in water and spectra collected after 30 minutes of aging, and (d) **NaU$_{24}$** dissolved in water with the DMPO spin trap agent.

additional analysis by EPR spectroscopy. When the clusters were dissolved in water and immediately measured on the EPR spectrometer (Fig. 5b), we observed an isotropic signature at g = 2.024. If a second EPR spectrum is recorded after aging the solution for 30 minutes, the signature disappears from the spectrum (Fig. 5c), and after 24 h., the sample remains EPR silent. This is different from what was previously observed for uranyl superoxide/peroxide phases, where no signature was initially observed, but an isotropic feature at g = 2.032 appeared after aging for several days.[18] A control experiment was also performed, where the EPR spectra were collected in solution with sodium superoxide at a pH of around 7 and no signal was observed, which is expected based on the half-life of the superoxide or other reactive oxygen species under these conditions.[87] This suggests that the radical is initially stabilized in solution for a short period of time, but then the species degrades rapidly in solution. When the cluster is dissolved in water with the DMPO spin trap present in the solution, then there is evidence of hydroxide radicals present in the sample (Fig. 5d). The hyperfine splitting constants that were measured (A_H = 14.89, A_G = 14.99) with a 1 : 2 : 2 : 1 splitting pattern were consistent with the previously reported DMPO-OH adduct in water as the solvent.[54] However, it is

unclear if this is caused by the presence of $^{•}$OH radicals in the original solid or the reactivity of HO$_2^{•}$ or H$_2$O$_2$ during dissolution.

DFT insights into observed radicals

To elucidate the experimental solid-state and solution-state EPR observations from the NaU$_{24}$ cluster, we turned to DFT calculations of related molecular models and calculated theoretical g values. First, we examined the potential stabilization of the superoxide anion within the uranyl peroxide cluster framework. Performing DFT calculations on the full U$_{24}$ cluster was deemed computationally prohibitive; therefore, we utilized two uranyl hydroxy peroxo dimers cleaved from the larger cluster (Fig. 6). The selection of dimers, rather than a larger oligomer, is supported by our prior studies on extended uranyl peroxides, such as studtite and metastudtite, where uranyl dimers were shown to provide accurate g-tensor calculations for the superoxide complexed with the uranyl cation.[18]

The first dimer, U-Dimer 1 (Fig. 6a), features two terminal peroxo groups on each uranyl center and two bridging hydroxyl groups. In contrast, U-Dimer 2 (Fig. 6b) contains two terminal
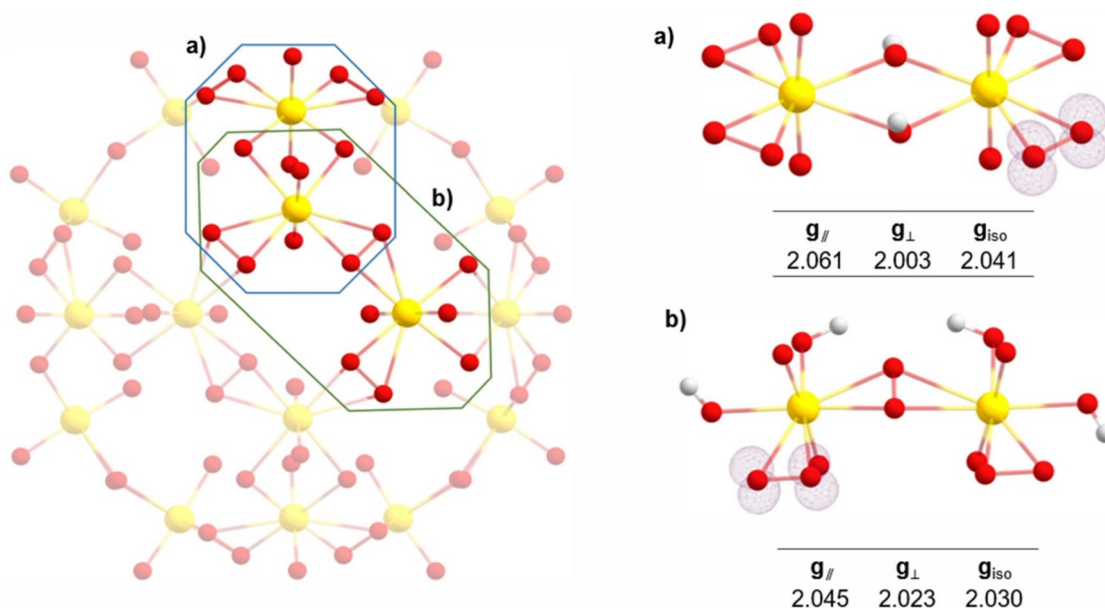
Fig. 6 Calculated g-factors and spin densities of uranyl hydroxo peroxide dimers cleaved for the U_{24} cluster were determined for (a) U-Dimer 1 and (b) U-Dimer 2, respectively. The isosurfaces of the spin densities were generated with a contour value of 0.015.

hydroxyl groups and one terminal peroxo group on each uranyl center, along with a bridging peroxo group. In both dimers, the removal of an electron results in the conversion of one of the terminal peroxo groups to a superoxide. The calculated g-tensor values for U-Dimer 1 and U-Dimer 2 exhibit axial signatures, with $g_{\parallel} = 2.061$, $g_{\perp} = 2.003$ and $g_{\parallel} = 2.045$, $g_{\perp} = 2.023$, respectively (Fig. 6). The shape and numerical values of the calculated g-tensors align well with previous experimental solid-state EPR measurements of superoxide stabilized within uranyl peroxide environments,[18] but the calculated values do not agree well with the results from the experimental EPR measurements of the NaU_{24} solid or solution.

It is also important to note that the formation of a bridging or terminal $^{\bullet}OH$ radical could not be achieved in any of the modeled actinyl compounds. In all cases, the unpaired spin density localized on a peroxide ligand, resulting in the formation of a superoxide anion. The only exception was observed in calculations performed on a uranyl hydroxide complex in the absence of peroxide ligands, $i.e.$, $[UO_2(OH)_4]^{\ast-}$. Even in

this case, the spin density was delocalized across the entire molecule rather than being confined to a specific hydroxo ligand (Fig. S8). These results further support the conclusion that the formation of a uranyl-coordinated hydroxyl radical is highly unlikely.

Next, we calculated the g-tensors of oxygen-based radicals that may be present within the crystal structure or in the adsorbed water on the crystal surface (Table 1). These radicals could reside within the cluster itself (occupying the internal space of the cluster) or in the interstitial spaces between clusters. Within the solid-state material, the experimental g_{iso} value for $HO_2^{\bullet}$ (2.019) is similar to the predicted value (2.014), and the previously reported experimental g_{iso} value for $HO_2^{\bullet}$ (2.016) is even closer to the experimental observation.[85,86] Differences between the calculated and the experimental values have previously been shown to be associated with variations in the second sphere coordination environment between the model and the actual compound.[88] The presence of an isotropic feature instead of the anisotropic signature

Table 1 Calculated and reported experimental g-factors of oxygen base radicals

Radical	Calculated			Experimentally reported		
	$g_{\parallel}$	$g_{\perp}$	g_{iso}	$g_{\parallel}$	$g_{\perp}$	g_{iso}
$O_2^{\bullet-}$	2.175	2.006	2.062	2.034–2.168[89]	2.005–2.075[90]	2.015–2.106[91]
$H_2O^{\bullet+}$	2.015	2.004	2.008	—	—	2.0093[92,93]
$HO^{\bullet}$	2.067	2.005	2.025	2.057–2.060[93]	2.003–2.009[93]	—
$HO_2^{\bullet}$	2.033	2.005	2.014	2.039	2.004	2.016[85]
$NaO_2^{\bullet}$	2.067	2.006	2.026	—	—	—
$SO_4^{\bullet-}$	2.005	2.017	2.013	2.0046[94]	2.0325[a][94]	—

[a] Irradiation of potassium persulfate to form $SO_4^{\bullet-}$ pairs.

usually observed for U(VI) compounds supports that the $HO_2^•$ is not coordinated to the actinide cation. Therefore, the computational results suggest that the hydroperoxyl radical observed from Raman and IR spectroscopy is either found within the Na^+ network or associated with surface-bound species on the crystal face.

Within the solution phase, the experimentally observed isotropic feature at 2.024 closely aligns with the calculated g_{iso} values of $HO^•$ (2.025) and $NaO_2^•$ (2.026). This suggests that hydroxyl radicals or superoxide radicals are released into solution when the crystals are dissolved in solution. The presence of $HO^•$ aligns with the EPR spectroscopy results, where signatures for DMPO-OH adducts were detected in the solution. However, the isotropic signature at $g = 2.025$ in solutions without DMPO suggests that it must be complexed to a metal, like U(VI) because the lifetime of free $^•OH$ in solution prohibits its detection without a spin trap. The challenge with dissolving crystals into the solution for EPR analysis is that there is breakdown of the lattice that can induce a wide range of reactivity, including degradation of the interstitial peroxide groups or decomposition of the U_{24} cluster into smaller molecular components. During this decomposition, it is possible that there is a U(VI) stabilized $^•OH$ or $HO_2^•$ species that can be analyzed by EPR spectroscopy without the DMPO spin trap before reacting to form a diamagnetic species.

This work has implications for understanding the behavior of U(VI) in the presence of free radicals produced by water radiolysis. We do not see evidence that the U(VI) coordinates with the sulfate radical under these conditions. Considering that formation coefficients ($\log B$) for the $UO_2(SO_4)^0$ range between 3.03 and 3.67, the decreased charge of $SO_4^{•-}$ would likely lower the favorability of this interaction further.[95] We also do not specifically observe the U(VI) coordination to the $^•OH$ radical in either experimental or computational data, which is somewhat surprising given that the formation constants for $UO_2(OH)^+$ are $\log B = 9.5$ at pH and 23.6 at pH 12[96] and it was previously suggested to exist within U(VI) peroxide clusters by Lottes et al.[16] However, the lower charge on the radical species compared to the OH^- anion may decrease the likelihood of binding or stabilization by the uranyl cation. Under these experimental conditions, the $^•OH$ radical can react to form H_2O_2, which does bind strongly to the U(VI) species and support the formation of the NaU_{24} cluster. However, the breakdown of NaU_{24} may also follow a pathway that forms $^•OH$ radicals, demonstrating the continuing cascade reactions that can occur from the formation of reactive oxygen species in these systems.

Conclusions

Overall, the persulfate initiator released both sulfate and hydroxide radicals that resulted in the formation of a U(VI) peroxide cluster through a radical cascade mechanism. We found no evidence that the sulfate or hydroxide radicals generated from the persulfate activation formed stable complexes with the U(VI). Instead, these species further reacted in solution to form a peroxide that complexed with U(VI) and formed a larger NaU_{24} species. Evidence of radicals was found in the solid-state materials using Raman, EPR, and IR spectroscopy, but the exact nature of the radicals was difficult to determine from these techniques. DFT was used to calculate predicted EPR signatures for both bound and free radical species and suggested that these species are associated with the sodium peroxide network or the surface of the material. Dissolution of NaU_{24} does result in the formation of additional $^•OH$ radicals, which we believe are formed from the reactivity of the $^•OH$ or $HO_2^•$ species in the presence of water.

Use of chemical initiators provides insights into how different radicals associated with water radiolysis may interact with actinides, but additional efforts are needed to confirm these interactions within high radiation fields. This study suggests that peroxide and potentially superoxide will outcompete hydroxide radicals for actinide binding, but this may be pH dependent and warrants further study. In addition, our results suggest that the breakdown of U(VI) peroxide clusters may induce the formation of other radicals in solution and result in secondary chemical reactions. However, in high radiation fields, the presence of solvated electrons and other highly reactive species may influence the overall behavior, and this cannot be accounted for with chemical initiators. Therefore, pairing radiation experiments with radical initiator studies and computational efforts offers the best options for obtaining a fundamental understanding of actinide behavior in high radiation fields.

Conflicts of interest

There are no conflicts to declare.

Data availability

The data supporting this article have been included as part of the SI. For crystallographic data, Raman spectra, infrared spectra, and DFT details, see DOI: **https://doi.org/10.1039/d5dt00785b**.

CCDC 2433767 contains the supplementary crystallographic data for this paper.[97]

Acknowledgements

References

1 L. Caër and S. Water, Radiolysis: Influence of Oxide Surfaces on H2 Production under Ionizing Radiation, *Water*, 2011, **3**(1), 235–253.

2 B. J. Mincher and S. P. Mezyk, Radiation chemical effects on radiochemistry: A review of examples important to nuclear power, *Radiochim. Acta*, 2009, **97**(9), 519–534, DOI: **10.1524/ract.2009.1646**.

3 H. Christensen and S. Sunder, Current State of Knowledge of Water Radiolysis Effects on Spent Nuclear Fuel Corrosion, *Nucl. Technol.*, 2000, **131**(1), 102–123, DOI: **10.13182/NT00-A3107**.

4 S. Sunder, D. W. Shoesmith and N. H. Miller, Oxidation and dissolution of nuclear fuel (UO2) by the products of the alpha radiolysis of water, *J. Nucl. Mater.*, 1997, **244**(1), 66–74, DOI: **10.1016/S0022-3115(96)00709-X**.

5 B. J. Mincher, The effects of radiation chemistry on radiochemistry: when unpaired electrons defy great expectations, *J. Radioanal. Nucl. Chem.*, 2018, **316**(2), 799–804, DOI: **10.1007/s10967-018-5728-1**.

6 B. J. Mincher, M. Giuseppe and S. P. Mezyk, Review Article: The Effects of Radiation Chemistry on Solvent Extraction: 1. Conditions in Acidic Solution and a Review of TBP Radiolysis, *Solvent Extr. Ion Exch.*, 2009, **27**(1), 1–25, DOI: **10.1080/07366290802544767**.

7 B. J. Mincher, Radiation chemistry in the reprocessing and recycling of spent nuclear fuels, in *Reprocessing and Recycling of Spent Nuclear Fuel*, ed. R. Taylor, Woodhead Publishing, 2015, ch. 8, pp. 191–211.

8 R. Springell, S. Rennie, L. Costelle, J. Darnbrough, C. Stitt, E. Cocklin, C. Lucas, R. Burrows, H. Sims, D. Wermeille, *et al.*, Water corrosion of spent nuclear fuel: radiolysis driven dissolution at the UO2/water interface, *Faraday Discuss.*, 2015, **180**, 301–311, DOI: **10.1039/C4FD00254G**.

9 K. Maher, J. R. Bargar and G. E. Brown Jr, Environmental Speciation of Actinides, *Inorg. Chem.*, 2013, **52**(7), 3510–3532, DOI: **10.1021/ic301686d**.

10 C. Walther and M. A. Denecke, Actinide Colloids and Particles of Environmental Concern, *Chem. Rev.*, 2013, **113**(2), 995–1015, DOI: **10.1021/cr300343c**.

11 K.-A. H. Kubatko, K. B. Helean, A. Navrotsky and P. C. Burns, Stability of Peroxide-Containing Uranyl Minerals, *Science*, 2003, **302**(5648), 1191–1193, DOI: **10.1126/science.1090259**.

12 B. McNamara, B. Hanson, E. Buck and C. Soderquist, A Radiochemical Analyses of Metastudtite and Leachates from Spent Fuel, *MRS Online Proc. Libr.*, 2004, **824**(1), 544–549, DOI: **10.1557/PROC-824-CC9.4**.

13 G. Sattonnay, C. Ardois, C. Corbel, J. F. Lucchini, M. F. Barthe, F. Garrido and D. Gosset, Alpha-radiolysis effects on UO2 alteration in water, *J. Nucl. Mater.*, 2001, **288**(1), 11–19, DOI: **10.1016/S0022-3115(00)00714-5**.

14 D. V. Kravchuk, N. N. Dahlen, S. J. Kruse, C. D. Malliakas, P. M. Shand and T. Z. Forbes, Isolation and Reactivity of

15 S. K. Scherrer, C. Gates, H. Rajapaksha, S. M. Greer, B. W. Stein and T. Z. Forbes, Superoxide Radicals in Uranyl Peroxide Solids: Lasting Signatures Identified by Electron Paramagnetic Resonance Spectroscopy, *Angew. Chem., Int. Ed.*, 2024, **63**(21), e202400379, DOI: **10.1002/anie.202400379**.

16 B. Lottes and K. P. Carter, Capture and Stabilization of the Hydroxyl Radical in a Uranyl Peroxide Cluster, *Chem. – Eur. J.*, 2023, **29**(45), e202300749, DOI: **10.1002/chem.202300749**.

17 D. V. Kravchuk and T. Z. Forbes, In Situ Generation of Organic Peroxide to Create a Nanotubular Uranyl Peroxide Phosphate, *Angew. Chem., Int. Ed.*, 2019, **58**(51), 18429–18433, DOI: **10.1002/anie.201910287**.

18 S. K. Scherrer, H. Rajapaksha, D. V. Kravchuk, S. E. Mason and T. Z. Forbes, Impacts of trace level chromium on formation of superoxide within uranyl triperoxide complexes, *Chem. Commun.*, 2024, **60**(76), 10584–10587, DOI: **10.1039/D4CC03194F**.

19 D. V. Kravchuk and T. Z. Forbes, Thermodynamics and Chemical Behavior of Uranyl Superoxide at Elevated Temperatures, *ACS Mater. Au*, 2022, **2**(1), 33–44, DOI: **10.1021/acsmaterialsau.1c00033**.

20 X. Chen, J. Wang, Y. Guo, H. Zeng, K. Xuan, Y. Guo, H. Jiang, X. Wang and Z. Zhou, Enhanced reduction of uranium(VI) in groundwater via regulation of heat-activated persulfate: The role of formate and its mechanisms, *J. Environ. Chem. Eng.*, 2023, **11**(5), 110299, DOI: **10.1016/j.jece.2023.110299**.

21 R. L. Johnson, P. G. Tratnyek and R. O. B. Johnson, Persulfate Persistence under Thermal Activation Conditions, *Environ. Sci. Technol.*, 2008, **42**(24), 9350–9356, DOI: **10.1021/es8019462**.

22 M. Izadifard, G. Achari and C. H. Langford, Degradation of sulfolane using activated persulfate with UV and UV-Ozone, *Water Res.*, 2017, **125**, 325–331, DOI: **10.1016/j.watres.2017.07.042**.

23 Y. Wu, R. Prulho, M. Brigante, W. Dong, K. Hanna and G. Mailhot, Activation of persulfate by Fe(III) species: Implications for 4-tert-butylphenol degradation, *J. Hazard. Mater.*, 2017, **322**, 380–386, DOI: **10.1016/j.jhazmat.2016.10.013**.

24 T. Huang, L. Zhou, Z. Cao, S. Zhang and L. Liu, A microwave irradiation-persulfate-formate system for achieving the detoxification and alkali-activated composite geopolymerization of the chromate-contaminated soil, *Ecotoxicol. Environ. Saf.*, 2021, **217**, 112233, DOI: **10.1016/j.ecoenv.2021.112233**.

25 M. C. R. Symons and S. B. Barnes, Unstable intermediates. Part LXXVI. An electron spin resonance study of radiation damage in persulphate crystals. Interconversion of S2O8− and SO5− radicals induced by light and heat, *J. Chem. Soc. A*, 1970, 2000–2002, DOI: **10.1039/J19700002000**.

26 G. Fang, W. Wu, C. Liu, D. D. Dionysiou, Y. Deng and D. Zhou, Activation of persulfate with vanadium species for

PCBs degradation: A mechanistic study, *Appl. Catal., B*, 2017, **202**, 1–11, DOI: 10.1016/j.apcatb.2016.09.006.

27 G. Sheldrick, Crystal structure refinement with SHELXL, *Acta Crystallogr., Sect. C:Struct. Chem.*, 2015, **71**(1), 3–8, DOI: 10.1107/S2053229614024218.

28 B. Thomsett-Scott, Software Review of Origin 8, *J. Chem. Inf. Model.*, 2009, **49**(8), 2010–2010, DOI: 10.1021/ci900198p.

29 M. J. Frisch, G. W. Trucks, H. B. Schlegel, G. E. Scuseria, M. A. Robb, J. R. Cheeseman, G. Scalmani, V. Barone, G. A. Petersson, H. Nakatsuji, *et al.*, *Gaussian 16*, 2009.

30 A. D. Becke, Density–functional thermochemistry. III. The role of exact exchange, *J. Chem. Phys.*, 1993, **98**(7), 5648–5652, DOI: 10.1063/1.464913.

31 C. Lee, W. Yang and R. G. Parr, Development of the Colle-Salvetti correlation-energy formula into a functional of the electron density, *Phys. Rev. B:Condens. Matter Mater. Phys.*, 1988, **37**(2), 785–789, DOI: 10.1103/PhysRevB.37.785.

32 S. Grimme, S. Ehrlich and L. Goerigk, Effect of the damping function in dispersion corrected density functional theory, *J. Comput. Chem.*, 2011, **32**(7), 1456–1465, DOI: 10.1002/jcc.21759.

33 F. Weigend, M. Häser, H. Patzelt and R. Ahlrichs, RI-MP 2: optimized auxiliary basis sets and demonstration of efficiency, *Chem. Phys. Lett.*, 1998, **294**(1), 143–152, DOI: 10.1016/S0009-2614(98)00862-8.

34 X. Cao and M. Dolg, Segmented contraction scheme for small-core actinide pseudopotential basis sets, *J. Mol. Struct.: THEOCHEM*, 2004, **673**(1), 203–209, DOI: 10.1016/j.theochem.2003.12.015.

35 X. Cao, M. Dolg and H. Stoll, Valence basis sets for relativistic energy-consistent small-core actinide pseudopotentials, *J. Chem. Phys.*, 2003, **118**(2), 487–496, DOI: 10.1063/1.1521431.

36 V. Barone and M. Cossi, Quantum Calculation of Molecular Energies and Energy Gradients in Solution by a Conductor Solvent Model, *J. Phys. Chem. A*, 1998, **102**(11), 1995–2001, DOI: 10.1021/jp9716997.

37 A. Klamt, Conductor-like Screening Model for Real Solvents: A New Approach to the Quantitative Calculation of Solvation Phenomena, *J. Phys. Chem.*, 1995, **99**(7), 2224–2235, DOI: 10.1021/j100007a062.

38 F. Neese, F. Wennmohs, U. Becker and C. Riplinger, The ORCA quantum chemistry program package, *J. Chem. Phys.*, 2020, **152**(22), 224108, DOI: 10.1063/5.0004608.

39 E. V. Lenthe, E.-J. Baerends and J. G. Snijders, Relativistic regular two–component Hamiltonians, *J. Chem. Phys.*, 1993, **99** (6), 4597–4610.

40 C. van Wüllen, Molecular density functional calculations in the regular relativistic approximation: Method, application to coinage metal diatomics, hydrides, fluorides and chlorides, and comparison with first-order relativistic calculations, *J. Chem. Phys.*, 1998, **109**(2), 392–399.

41 D. A. Pantazis, X.-Y. Chen, C. R. Landis and F. Neese, All-electron scalar relativistic basis sets for third-row transition metal atoms, *J. Chem. Theory Comput.*, 2008, **4**(6), 908–919.

42 F. Weigend and R. Ahlrichs, Balanced basis sets of split valence, triple zeta valence and quadruple zeta valence quality for H to Rn: Design and assessment of accuracy, *Phys. Chem. Chem. Phys.*, 2005, **7**(18), 3297–3305.

43 D. A. Pantazis and F. Neese, All-Electron Scalar Relativistic Basis Sets for the Actinides, *J. Chem. Theory Comput.*, 2011, **7**(3), 677–684, DOI: 10.1021/ct100736b.

44 Chemcraft, 2009. https://www.chemcraftprog.com (accessed).

45 A. Behnami, E. Aghayani, K. Z. Benis, M. Sattari and M. Pourakbar, Comparing the efficacy of various methods for sulfate radical generation for antibiotics degradation in synthetic wastewater: degradation mechanism, kinetics study, and toxicity assessment, *RSC Adv.*, 2022, **12**(23), 14945–14956, DOI: 10.1039/D2RA01618D.

46 J. Wang, W. Zheng, Y. Zhang, S. Song, I. M. Chou, M. Hu and Z. Pan, Raman spectroscopic technique towards understanding the degradation of phenol by sodium persulfate in hot compressed water, *Chemosphere*, 2020, **257**, 127264, DOI: 10.1016/j.chemosphere.2020.127264.

47 O. S. Furman, A. L. Teel and R. J. Watts, Mechanism of Base Activation of Persulfate, *Environ. Sci. Technol.*, 2010, **44**(16), 6423–6428, DOI: 10.1021/es1013714.

48 M. C. Bayer, C. Jessen and A. J. Kornath, Preparation and Characterization of Protonated Fumaric Acid, *Z. fur Anorg. Allg. Chem.*, 2020, **646**(7), 333–339, DOI: 10.1002/zaac.202000091.

49 C. Nguyen Trung, G. M. Begun and D. A. Palmer, Aqueous uranium complexes. 2. Raman spectroscopic study of the complex formation of the dioxouranium(VI) ion with a variety of inorganic and organic ligands, *Inorg. Chem.*, 1992, **31**(25), 5280–5287, DOI: 10.1021/ic00051a021.

50 T. H. L. Jahinge, D. K. Unruh and T. Z. Forbes, Heterometallic Uranyl (Hydroxyethyl)iminodiacetic Acid (Heidi) Complexes: Molecular Models for U(VI) Uptake in Complex Media, *Eur. J. Inorg. Chem.*, 2023, **26**(11), e202200791, DOI: 10.1002/ejic.202200791.

51 D. V. Kravchuk, A. Blanes Diaz, M. E. Carolan, E. A. Mpundu, D. M. Cwiertny and T. Z. Forbes, Uranyl Speciation on the Surface of Amidoximated Polyacrylonitrile Mats, *Inorg. Chem.*, 2020, **59**(12), 8134–8145, DOI: 10.1021/acs.inorgchem.0c00440.

52 G. Lu, A. J. Haes and T. Z. Forbes, Detection and identification of solids, surfaces, and solutions of uranium using vibrational spectroscopy, *Coord. Chem. Rev.*, 2018, **374**, 314–344, DOI: 10.1016/j.ccr.2018.07.010.

53 P. Yang, Y. Ji, J. Lu and Q. Huang, Formation of Nitrophenolic Byproducts during Heat-Activated Peroxydisulfate Oxidation in the Presence of Natural Organic Matter and Nitrite, *Environ. Sci. Technol.*, 2019, **53**(8), 4255–4264, DOI: 10.1021/acs.est.8b06967.

54 G. R. Buettner, Spin Trapping: ESR parameters of spin adducts 1474 1528 V, *Free Radicals Biol. Med.*, 1987, **3**(4), 259–303, DOI: 10.1016/S0891-5849(87)80033-3.

55 S. Yan, X. Zhang and H. Zhang, Persulfate activation by Fe (III) with bioelectricity at acidic and near-neutral pH

regimes: Homogeneous versus heterogeneous mechanism, *J. Hazard. Mater.*, 2019, **374**, 92–100, DOI: **10.1016/j.jhazmat.2019.03.068**.

56 S. K. Jackson, M. P. Thomas, S. Smith, M. Madhani, S. C. Rogers and P. E. James, In vivo EPR spectroscopy: biomedical and potential diagnostic applications, *Faraday Discuss.*, 2004, **126**(0), 103–117, DOI: **10.1039/B307162F**.

57 D. A. House, Kinetics and Mechanism of Oxidations by Peroxydisulfate, *Chem. Rev.*, 1962, **62**(3), 185–203, DOI: **10.1021/cr60217a001**.

58 I. M. Kolthoff and I. K. Miller, The Chemistry of Persulfate. I. The Kinetics and Mechanism of the Decomposition of the Persulfate Ion in Aqueous Medium1, *J. Am. Chem. Soc.*, 1951, **73**(7), 3055–3059, DOI: **10.1021/ja01151a024**.

59 G. V. Buxton, S. McGowan, G. A. Salmon, J. E. Williams and N. D. Wood, A study of the spectra and reactivity of oxysulphur-radical anions involved in the chain oxidation of S(IV): A pulse and γ-radiolysis study, *Atmos. Environ.*, 1996, **30**(14), 2483–2493, DOI: **10.1016/1352-2310(95)00473-4**.

60 C. Jégou, B. Muzeau, V. Broudic, S. Peuget, A. Poulesquen and D. Roudil, Effect of External Gamma Irradiation on Dissolution of the UO2 Matrix, *MRS Online Proc. Libr.*, 2004, **824**(1), 550–556, DOI: **10.1557/PROC-824-CC9.5**.

61 Y. Zhu, Y. Liu, P. Li, Y. Zhang, G. Wang and Y. Zhang, A comparative study of peroxydisulfate and peroxymonosulfate activation by a transition metal–H2O2 system, *Environ. Sci. Pollut. Res.*, 2021, **28**(34), 47342–47353, DOI: **10.1007/s11356-021-13982-8**.

62 S. G. Thangavelu and C. L. Cahill, Uranyl-Promoted Peroxide Generation: Synthesis and Characterization of Three Uranyl Peroxo [(UO2)2(O2)] Complexes, *Inorg. Chem.*, 2015, **54**(9), 4208–4221, DOI: **10.1021/ic502767k**.

63 J. A. Nieweg, K. Lemma, B. G. Trewyn, V. S. Y. Lin and A. Bakac, Mesoporous Silica-Supported Uranyl: Synthesis and Photoreactivity, *Inorg. Chem.*, 2005, **44**(16), 5641–5648, DOI: **10.1021/ic050130e**.

64 W.-D. Wang, A. Bakac and J. H. Espenson, Uranium(VI)-Catalyzed Photooxidation of Hydrocarbons with Molecular Oxygen, *Inorg. Chem.*, 1995, **34**(24), 6034–6039, DOI: **10.1021/ic00128a014**.

65 K.-X. Wang and J.-S. Chen, Extended Structures and Physicochemical Properties of Uranyl–Organic Compounds, *Acc. Chem. Res.*, 2011, **44**(7), 531–540, DOI: **10.1021/ar200042t**.

66 A. S. Jayasinghe, L. C. Applegate, D. K. Unruh, J. Hutton and T. Z. Forbes, Utilizing Autoxidation of Solvents To Promote the Formation of Uranyl Peroxide Materials, *Cryst. Growth Des.*, 2019, **19**(3), 1756–1766, DOI: **10.1021/acs.cgd.8b01735**.

67 D. K. Unruh, A. Burtner, L. Pressprich, G. E. Sigmon and P. C. Burns, Uranyl peroxide closed clusters containing topological squares, *Dalton Trans.*, 2010, **39**(25), 5807–5813, DOI: **10.1039/C0DT00074D**.

68 P. C. Burns, K.-A. Kubatko, G. Sigmon, B. J. Fryer, J. E. Gagnon, M. R. Antonio and L. Soderholm, Actinyl

Peroxide Nanospheres, *Angew. Chem., Int. Ed.*, 2005, **44**, 2135–2139, DOI: **10.1002/anie.200462445**.

69 P. A. Julien, G. Castle, J. Theriault, T. A. Kohlgruber, A. G. Oliver and P. C. Burns, Assembly of Uranyl Peroxides from Ball Milled Solids, *Inorg. Chem.*, 2022, **61**(29), 11319–11324, DOI: **10.1021/acs.inorgchem.2c01445**.

70 H. L. Lobeck, H. Traustason, P. A. Julien, J. R. FitzPatrick, S. Mana, J. E. S. Szymanowski and P. C. Burns, In situ Raman spectroscopy of uranyl peroxide nanoscale cage clusters under hydrothermal conditions, *Dalton Trans.*, 2019, **48**(22), 7755–7765, DOI: **10.1039/C9DT01529A**.

71 B. T. McGrail, G. E. Sigmon, L. J. Jouffret, C. R. Andrews and P. C. Burns, Raman Spectroscopic and ESI-MS Characterization of Uranyl Peroxide Cage Clusters, *Inorg. Chem.*, 2014, **53**(3), 1562–1569, DOI: **10.1021/ic402570b**.

72 J. Xie, H. A. Neal, J. Szymanowski, P. C. Burns, T. M. Alam, M. Nyman and L. Gagliardi, Resolving Confined 7Li Dynamics of Uranyl Peroxide Capsule U24, *Inorg. Chem.*, 2018, **57**(9), 5514–5525, DOI: **10.1021/acs.inorgchem.8b00474**.

73 M. Nyman and T. M. Alam, Dynamics of Uranyl Peroxide Nanocapsules, *J. Am. Chem. Soc.*, 2012, **134**(49), 20131–20138, DOI: **10.1021/ja308673f**.

74 T. M. Alam, Z. Liao, L. N. Zakharov and M. Nyman, Solid-State Dynamics of Uranyl Polyoxometalates, *Chem. – Eur. J.*, 2014, **20**(27), 8302–8307, DOI: **10.1002/chem.201402351**.

75 P. L. Zanonato, P. Bernardo, A. Fischer and I. Grenthe, Chemical equilibria in the UO2²⁺-H2O2-F⁻/OH⁻ systems and possible solution precursors for the formation of [Na6(OH2)8]@[UO2(O2)F]24¹⁸⁻ and [Na6(OH2)8]@[UO2(O2)OH]24¹⁸⁻ clusters, *Dalton Trans.*, 2013, **42**, 10129–10137.

76 D. E. Felton, M. Fairley, A. Arteaga, M. Nyman, J. A. LaVerne and P. C. Burns, Gamma-Ray-Induced Formation of Uranyl Peroxide Cage Clusters, *Inorg. Chem.*, 2022, **61**(30), 11916–11922, DOI: **10.1021/acs.inorgchem.2c01657**.

77 H. H. Eysel and S. D. Thym, RAMAN Spectra of Peroxides, *Z. fur Anorg. Allg. Chem.*, 1975, **411**, 97–102.

78 L. Andrews, Matrix infrared spectrum and bonding in the lithium superoxide molecule, LiO2, *J. Am. Chem. Soc.*, 1968, **90**(26), 7368–7370, DOI: **10.1021/ja01028a048**.

79 M. Hayyan, M. A. Hashim and I. M. AlNashef, Superoxide Ion: Generation and Chemical Implications, *Chem. Rev.*, 2016, **116**(5), 3029–3085, DOI: **10.1021/acs.chemrev.5b00407**.

80 U. Stoin, A. I. Shames, I. Malka, I. Bar and Y. Sasson, In situ Generation of Superoxide Anion Radical in Aqueous Medium under Ambient Conditions, *ChemPhysChem*, 2013, **14**(18), 4158–4164, DOI: **10.1002/cphc.201300707**.

81 D. W. Smith and L. Andrews, Argon matrix infrared spectra and vibrational analysis of the hydroperoxyl and deuteroperoxyl free radicals, *J. Chem. Phys.*, 1974, **60**(1), 81–85, DOI: **10.1063/1.1680809**.

82 J. L. Arnau, P. A. Giguère, M. Abe and R. C. Taylor, Vibrational spectra and normal coordinate analysis of crystalline H2O2, D2O2, and HDO2, *Spectrochim. Acta, Part A*, 1974, **30**(3), 777–796, DOI: **10.1016/0584-8539(74)80196-0**.

83 M. Fairley, N. M. Myers, J. E. S. Szymanowski, G. E. Sigmon, P. C. Burns and J. A. LaVerne, Stability of

Solid Uranyl Peroxides under Irradiation, *Inorg. Chem.*, 2019, **58**(20), 14112–14119, DOI: **10.1021/acs.inorgchem.9b02132**.

84 E. W. Neuman, Potassium Superoxide and the Three–Electron Bond, *J. Chem. Phys.*, 1934, **2**(1), 31–33, DOI: **10.1063/1.1749353**.

85 F. J. Adrian, E. L. Cochran and V. A. Bowers, ESR Spectrum of HO2 in Argon at 4.2°K, *J. Chem. Phys.*, 1967, **47**(12), 5441–5442, DOI: **10.1063/1.1701813**.

86 S. Radhakrishna, B. V. R. Chowdari and A. Kasi Viswanath, EPR studies of the hydroperoxy radical in x-irradiated single crystals of $BaCl_2 \cdot 2H_2O$, *Chem. Phys. Lett.*, 1976, **40**(1), 134–138, DOI: **10.1016/0009-2614(76)80136-4**.

87 E. Finkelstein, G. M. Rosen and E. J. Rauckman, Spin trapping of superoxide and hydroxyl radical: Practical aspects, *Arch. Biochem. Biophys.*, 1980, **200**(1), 1–16, DOI: **10.1016/0003-9861(80)90323-9**.

88 S. J. Kruse, H. Rajapaksha, J. A. LaVerne, S. E. Mason and T. Z. Forbes, Radiation-Induced Defects in Uranyl Trinitrate Solids, *Chem. – Eur. J.*, 2024, **30**(35), e202400956, DOI: **10.1002/chem.202400956**.

89 M. Che and Z. Sojka, Electron transfer processes at the surface of $MoOx/SiO_2$ catalysts, *Top. Catal.*, 2001, **15**(2), 211–217, DOI: **10.1023/A:1016601815952**.

90 K. Sobańska, A. Krasowska, T. Mazur, K. Podolska-Serafin, P. Pietrzyk and Z. Sojka, Diagnostic Features of EPR Spectra of Superoxide Intermediates on Catalytic Surfaces and Molecular Interpretation of Their g and A Tensors, *Top. Catal.*, 2015, **58**(12), 796–810, DOI: **10.1007/s11244-015-0420-y**.

91 P. Pietrzyk, K. Podolska, T. Mazur and Z. Sojka, Heterogeneous Binding of Dioxygen: EPR and DFT Evidence for Side-On Nickel(II)–Superoxo Adduct with Unprecedented Magnetic Structure Hosted in MFI Zeolite, *J. Am. Chem. Soc.*, 2011, **133**(49), 19931–19943, DOI: **10.1021/ja208387q**.

92 L. B. Knight Jr and J. Steadman, ESR investigations of H_2O+, HDO+, D_2O+, and H217O+ isolated in neon matrices at 4 K, *J. Chem. Phys.*, 1983, **78**(10), 5940–5945, DOI: **10.1063/1.444601**.

93 J. E. Johnson and G. C. Moulton, ESR study of ice irradiated at 4.2 K, a thermally reversible radical, *J. Chem. Phys.*, 1978, **69**(7), 3108–3111, DOI: **10.1063/1.437002**.

94 M. Çemberci, R. Bıyık, M. Fidan and R. Tapramaz, EPR Study of UV and gamma irradiated potassium persulfate: A Sensitive dosimeter, *Radiat. Meas.*, 2021, **146**, 106616, DOI: **10.1016/j.radmeas.2021.106616**.

95 C. D. Alcorn, J. S. Cox, L. M. S. G. A. Applegarth and P. R. Tremaine, Investigation of Uranyl Sulfate Complexation under Hydrothermal Conditions by Quantitative Raman Spectroscopy and Density Functional Theory, *J. Phys. Chem. B*, 2019, **123**(34), 7385–7409, DOI: **10.1021/acs.jpcb.9b01544**.

96 I. Grenthe, X. Gaona, A. Plyasunov, L. Rao, W. Runde, B. Grambow, R. Konings, A. Smith and E. Moore, Second Update on the Chemical Thermodynamics of U, Np, Pu, Am and Tc, in *Chemical Thermodynamics*, 2020, Vol. 14.

97 T. Z. Forbes, V. Samarasiri and H. Rajapaksha, CCDC 2433767: Experimental Crystal Structure Determination, 2025, DOI: **10.5517/ccdc.csd.cc2mpjmh**.